

Lawrence Berkeley National Laboratory

Recent Work

Title

Growth of Lithium Dendrites and Globules through a Solid Block Copolymer Electrolyte as a Function of Current Density

Permalink

<https://escholarship.org/uc/item/4wx7223b>

Journal

Journal of Physical Chemistry C, 122(47)

ISSN

1932-7447

Authors

Maslyn, JA
Loo, WS
McEntush, KD
[et al.](#)

Publication Date

2018-11-29

DOI

10.1021/acs.jpcc.8b06355

Peer reviewed

**1Growth of Lithium Dendrites and Globules through a Solid Block Copolymer Electrolyte as a
2Function of Current Density**

3Jacqueline A. Maslyn ^{a,b}, Whitney S. Loo ^a, Kyle D. McEntush ^a, Hee Jeung Oh ^a, Katherine J. Harry ^{b,c},
4Dilworth Y. Parkinson ^d, Nitash P. Balsara ^{a,b,c,*}

5^a Department of Chemical and Biomolecular Engineering, University of California, Berkeley, California
694720, USA

7^b Materials Sciences Division, Lawrence Berkeley National Laboratory, Berkeley, California, 94720,
8USA

9^c Department of Materials Science and Engineering, University of California, Berkeley, California
1094720, USA

11^d Advanced Light Source, Lawrence Berkeley National Laboratory, Berkeley, California 94720, USA

12^e Energy Technologies Area, Lawrence Berkeley National Laboratory, Berkeley, California 94720, USA

13

14* Corresponding author. E-mail: nbalsara@berkeley.edu, Phone: 1-510-642-8973.

15

1

2ABSTRACT

3The uncontrollable non-planar electrodeposition of lithium is a significant barrier to the widespread
4adoption of high energy density rechargeable batteries with a lithium metal anode. A promising
5approach for preventing the growth of lithium dendrites is the use of solid polymer electrolytes with a
6high shear modulus. Current density is the key variable in the electrodeposition of lithium. The present
7study is the first attempt at quantifying the effect of current density on the geometry and density of
8dendrites and other protrusions during electrodeposition through a solid polymer electrolyte. The
9geometry and density of defects formed on the lithium electrode were determined by X-ray
10microtomography. The tomograms revealed protrusions on the electrodeposited lithium electrodes that
11were either globular or dendritic, or void defects. The range of current densities over which stable,
12planar deposition was observed is quantified. At higher current densities, globular protrusions were
13observed. At the highest current density, both globular and dendritic protrusions were observed. The
14areal density of protrusion defects increased sharply with current density, while the overall defect
15density is a weak function of current density. Our work enables comparisons between the
16experimentally determined onset of non-planar electrodeposition and prevailing theoretical predictions
17with no adjustable parameters.

18

1

1 INTRODUCTION

2 Rechargeable batteries are indispensable in the emerging clean energy landscape; especially relevant
3 will be safe, high energy density batteries necessary for the next generations of electric vehicles.^{1,2}
4 Batteries that incorporate a solid lithium anode have drawn interest for their significant improvements
5 over Li-ion gravimetric and volumetric energy density.³⁻⁵ In addition, a lithium metal anode is necessary
6 to enable battery chemistries like Li-sulfur and Li-oxygen, which have theoretical energy densities
7 comparable to that of octane.⁶ However, a longstanding challenge in rechargeable lithium metal
8 batteries is a tendency to fail due to the growth of protruding lithium dendrites from the metal anode as
9 the battery is charged.⁷⁻⁹ A promising approach for preventing the growth of lithium dendrites is through
10 the use of solid polymer electrolytes with a high shear modulus.

11 Lithium dendrites, and the analogous globules observed in solid polymer electrolytes, are a
12 manifestation of uneven current density at the electrode. It is apparent that the formation of lithium
13 dendrites is affected by current density, yet we know of no systematic studies of the effect of current
14 density on their density and morphology in solid polymer electrolytes. Current density has been shown
15 to affect lithium deposition morphology in organic liquid^{10,11} and liquid polymer electrolytes¹²⁻¹⁵, as well
16 as solid inorganic electrolytes.^{16,17} Liquid electrolytes do not have an appreciable shear modulus to
17 counteract the driving forces for lithium dendrite propagation. Inorganic solid electrolytes exhibit a
18 dendritic growth mechanism dependent along grain boundaries.¹⁸ Many previous studies on this subject
19 are restricted to an idealized geometry to accommodate visualization by optical microscopy with several
20 hundred microns between working and counter electrode.¹²⁻¹⁵ Electrodeposition of lithium on lithium
21 with an interelectrode distance on the order of tens of microns is more relevant to rechargeable batteries.
22 In the field of solid polymer electrolytes, there have been few studies wherein lithium dendrite growth

1has been studied as a function of a single parameter.^{19,20} Most studies in the literature report on the
2development of new electrolytes and demonstrate improved performance at a fixed current density.^{20–26}
3 In this paper, we study the effect of current density on the electrochemical deposition of lithium metal
4through a solid block copolymer electrolyte. In addition to electrochemical characterization, we use the
5non-invasive technique of synchrotron X-ray tomography to determine the nature and density of
6protrusions created by electrodeposition. The electrolyte is a nanostructured polystyrene-*block*-
7poly(ethylene oxide) (PS-*b*-PEO, or SEO) block copolymer in which lithium
8bis(trifluoromethanesulfone)imide (LiTFSI) salt is dissolved. This solid electrolyte comprises
9alternating c.a. 60 nm thick PS-rich and PEO-rich lamellae. LiTFSI selectively partitions to the PEO-
10rich lamellae.²⁷ This electrolyte combines two desired properties that are ordinarily mutually exclusive:
11soft PEO domains solvate and conduct lithium ions, while stiff PS domains lend mechanical rigidity to
12the solid electrolyte. The effect of mechanical rigidity on lithium deposition was first modeled in
13pioneering work by Monroe and Newman.^{28,29} More recent work by Barai et al. has elucidated the effect
14of current density and mechanical rigidity on lithium deposition.^{30,31} Notably, Barai et al. identified
15regimes of dendritic and non-dendritic lithium deposition as a function of current density and electrolyte
16modulus. Our approach allows for an experimental test of this theory with no adjustable parameters.

17

18EXPERIMENTAL SECTION

19 *Anionic synthesis and polymer purification.* The polystyrene-*block*-poly(ethylene oxide) (SEO)
20diblock copolymer was synthesized via sequential high-vacuum living anionic polymerization, using
21*sec*-butyllithium as the initiator for styrene polymerization and P4 *tert*-butylphosphazene base as the
22promoter for the polymerization of ethylene oxide.^{32–34} Trace impurities encountered before the ethylene
23oxide extension step resulted in dead polystyrene homopolymer chains. Polymers were precipitated in

1hexanes and then decanted to remove residual small molecules that originated from the synthesis
 2process. The polymers were then re-dissolved in benzene and precipitated two times in hexanes. Then,
 3polymers were subjected to an additional purification step to remove excess polystyrene homopolymer
 4using cyclohexane, in which PS has limited solubility and PEO is not soluble. First, the polymer was re-
 5dissolved in benzene and precipitated in a mixture of hexanes and cyclohexane. The precipitate was
 6isolated and stirred in cyclohexane at room temperature. Then, the process was repeated until gel
 7permeation chromatography (GPC) measurements indicated polymer with a unimodal size distribution.
 8The relevant properties of the SEO copolymer used in this study are provided in Table 1, where ϕ_{EO}
 9refers to the volume fraction of PEO. GPC was conducted on an Agilent 1260 Infinity Series fitted with
 10Water Styragel HR 3 and 4 columns. The polydispersity index (PDI) was measured as 1.1 using a
 11polystyrene standard. The morphology of the block copolymer is lamellar by volume fraction with an
 12approximate domain spacing of 120 nm.

13 _____

14 **Table 1. Properties of the polymer used in this study.**

<i>Name</i>	<i>M_{PS} [kg/mol]</i>	<i>M_{PEO} [kg/mol]</i>	<i>ϕ_{EO}</i>
SEO(115-172)	115	172	0.59

16
 17Methods for electrolyte preparation and electrochemical cell fabrication closely mimic those previously
 18reported by Harry et al. and Schauer et al.^{19,35–37} All electrolyte preparation was carried out in an argon
 19glove box with less than 2.5 parts per million (ppm) H₂O and less than 2 ppm O₂. All lithium cell
 20assembly was carried out in an argon glove box with less than 5 ppm H₂O and less than 8 ppm O₂.

21 *Li-SEO-Li symmetric cell assembly for polarization and tomographic imaging.* — Lithium metal foil
 22was purchased from FMC Lithium at 99.9% purity. The foil thickness was 150 μm. All sample
 23preparation was performed in a glove box filled with Argon gas. A 1/2 or 7/16-inch diameter metal

1 punch was used to cut a polymer electrolyte disc from the previously cast electrolyte film. Three layers
2 of lithium metal foil were stacked on top of a piece of nickel foil, and then pressed at 130 MPa until flat
3 and shiny inside pouch material with a pneumatic press. The lithium electrodes were made by using a
4 7/16 or 3/8-inch punch to cut through the three layers of lithium foil and nickel foil backing. The two,
5 450 μm thick, lithium electrodes were used to sandwich the polymer electrolyte membrane. Two 0.25
6 mm thick stainless steel shims were placed above and beneath the cell to keep the cell flat. Aluminum
7 current collector tabs were then affixed to the stainless steel shims and the sample was vacuum sealed in
8 polypropylene-lined aluminum pouch material.

9 *Conditioning and polarization.* Cells were galvanostatically cycled or polarized in an Associated
10 Environmental Systems SD-402 oven using a Maccor Series 4000 Battery Tester. Cells were allowed to
11 equilibrate at the temperature of interest for at least an hour before a current was imposed. Cells were
12 occasionally paused during conditioning or polarization for practical reasons (e.g., while removing a
13 failed cell). Each cell was subjected to fourteen conditioning cycles at 90 $^{\circ}\text{C}$. During each cycle, a
14 current density of 0.02 mA cm^{-2} was imposed in one direction for 4 hours, followed by a 45 min rest
15 period, followed by the imposition of a constant current density of 0.02 mA cm^{-2} in the opposite
16 direction, followed by another 45 min rest period. The thickness of lithium transferred between the
17 electrodes in each half cycle at 0.02 mA cm^{-2} was 0.4 μm . Cells were then polarized with various current
18 densities at 90 $^{\circ}\text{C}$ between 0.04 mA cm^{-2} and 0.64 mA cm^{-2} until a sudden drop in the voltage required
19 to maintain the target current density was observed. This was taken as the signature of a dendrite short.

20 *Linear rheology measurements.* A neat polymer sample disk of diameter 8 mm and thickness 0.6 mm
21 (final thickness after applying normal force) was prepared according to the method described by
22 Schauer et al.¹⁹ Temperatures used for measurements were 120, 110, 100, and 90 $^{\circ}\text{C}$. Due to limited

1material, only one sample was made but measurements at 90 and 100 °C, at and near the temperature of
2interest, were repeated multiple times.

3 *X-ray microtomography.* The cells were imaged using hard X-ray microtomography at the Advanced
4Light Source at Lawrence Berkeley National Laboratory. Monochromatic hard X-rays with energy 22
5keV at beamline 8.3.2 at the Advanced Light Source at Lawrence Berkeley National Laboratory
6illuminated the entire sample, and the X-ray shadow cast by the sample was converted into visible light
7using a scintillator. An optical microscope magnified this image and converted it into a digital image
8file. The sample was then rotated by a fraction of a degree and repeatedly imaged until 1,025 images
9were collected from the sample as it was rotated through 180°. After a series of data processing steps
10using the software Xi-Cam, these shadow images were converted to cross-sectional slices that were then
11stacked together to render a 3D reconstruction of the cell. Cells were not removed from their original
12pouching configuration before being imaged at 2x and/or 5x magnification, corresponding to a pixel
13size of approximately 3.25 μm or 1.3 μm, respectively. Cross-sectional slices were stacked and rendered
14by the software ImageJ to be inspected for features of interest. Reconstructed three dimensional (3D)
15images were analyzed using the commercially available Avizo software package. Data acquisition and
16analysis builds on methods described by Harry et al. ³⁵

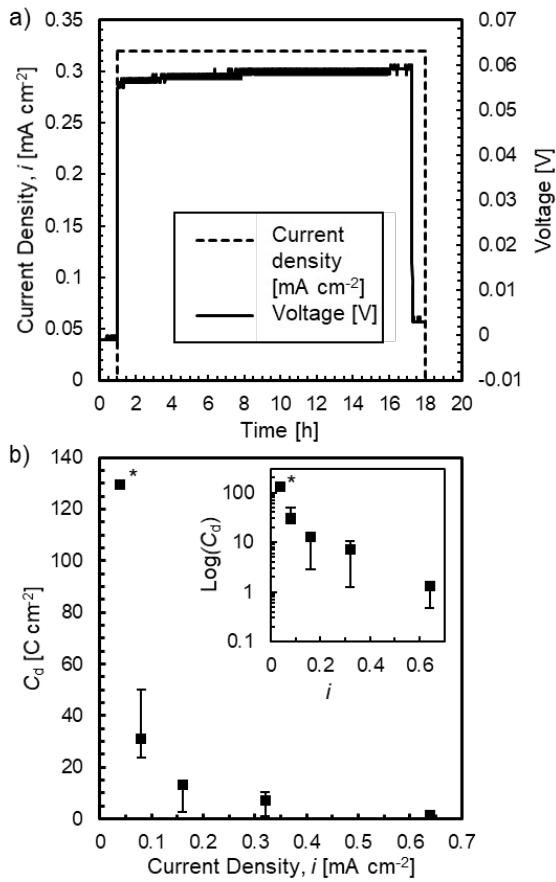
17

18RESULTS AND DISCUSSION

19 Each lithium-polymer-lithium cell was first conditioned identically at a low current density as
20described in the methods section, then galvanostatically polarized at a fixed current density of interest
21until the cell failed by short circuit. Figure 1a shows typical voltage versus time data obtained during
22polarization. After one hour of equilibration at 90 °C, a current density, i , of 0.32 mA/cm² was imposed
23on this cell. The resulting voltage, shown in Figure 1a, was nearly constant for about 17 hours, after

1 which a precipitous drop in voltage occurred, indicating cell failure by short circuit. Following short
2 circuit failure, the current flow was halted and the cell was imaged. For all cells, charge was passed in
3 only one direction, as shown in Figure 1a. Experiments of this type were repeated at several current
4 densities ranging from 0.04 to 0.64 mA cm⁻², and the results are shown in Figure 1b on a plot of C_d
5 versus i . The charge passed before failure, C_d , is calculated using the time of failure and the imposed
6 current density. It is evident that C_d is a sensitive function of i , decreasing monotonically as i is
7 increased from 0.08 to 0.64 mA cm⁻². The asterisk in Figure 1b at 0.04 mA cm⁻² indicates these cells did
8 not fail in spite of galvanostatic polarization for 900 hours. Thus, the reported value of C_d at this current
9 density may be considered as the lower limit.

10 Figure 2 shows a cross section of a polarized cell acquired using X-ray tomography. This cell was
11 polarized at $i = 0.04$ mA cm⁻² for 900 h. Under these conditions, a large fraction of the lithium in the top
12 electrode was deposited onto the bottom electrode – the thickness of the deposited lithium layer is
13 calculated to be 175 μm. The measured height of electrodeposited lithium is about 190 μm. The bright
14 band near the top of the cross section in Fig. 2 represents the electrolyte. Also shown in Fig. 2 is the
15 approximate location of the lithium-polymer interface at the initial time, $t = 0$. Only planar lithium
16 electrodeposition was observed in this cell – no protruding features were discernable on the bottom
17 electrode. Thus, we have evidence of a low current density regime where dendrite nucleation and
18 growth is entirely suppressed.



1

2 Figure 1. Data obtained from galvanostatically polarized lithium-polymer-lithium
 3symmetric cells. (a) Typical voltage versus time profile. The dashed line gives the applied
 4current density, i , and the solid line gives the voltage response, V . The sudden drop in
 5voltage at $t = 17$ h is indicative of a short circuit failure due to the growth of lithium
 6protrusions. (b) The average charge passed per area before failure, C_d , versus applied
 7current density, i . C_d decreases dramatically with increasing current density. The asterisk
 8at $i = 0.04 \text{ mA cm}^{-2}$ indicates these cells had not failed at the time point used to calculate
 9 C_d , ($t = 900$ h). The inset rescales the y-axis to logarithmic.

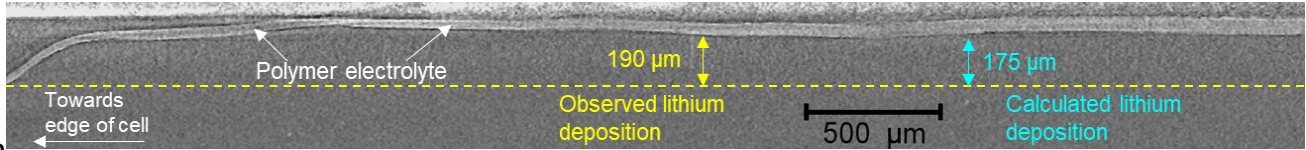
10

11

1

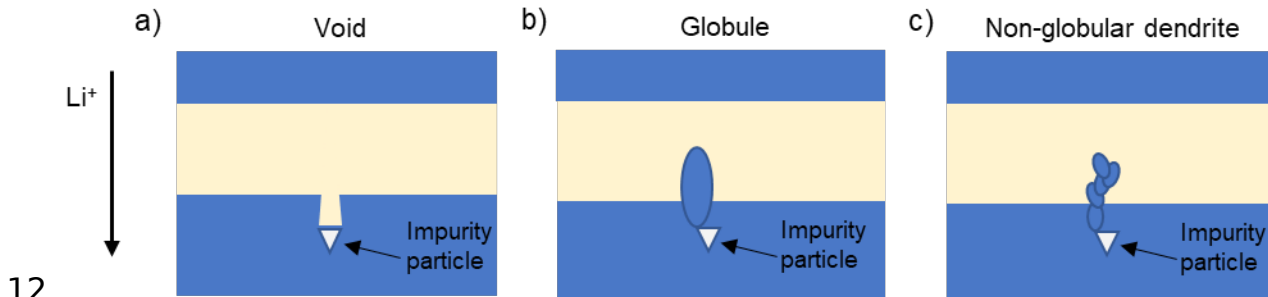
1

2



3

4 **Figure 2.** Representative cross section of cell polarized at $i = 0.04 \text{ mA cm}^{-2}$ for $t = 900 \text{ h}$ acquired using
5 X-ray tomography. Lithium was deposited downward through the polymer electrolyte, which appears as
6 a light band extending across the cell near the top of the cross-section. No lithium protrusions were
7 observed. This cell did not short circuit. The yellow arrow shows the thickness of the electrochemically
8 deposited lithium, $190 \text{ }\mu\text{m}$, at a representative location based on the analysis of the tomograms, using
9 the electrolyte's original position at the edge of the cell as a reference point. The blue arrow shows for
10 comparison the estimated thickness of electrochemically deposited lithium, $175 \text{ }\mu\text{m}$, based on the
11 current passed through the cell.



12

13

14 **Figure 3.** A schematic showing the three types of defects observed in this study: (a) a void defect, (b) a
15 protruding lithium globule, and (c) a protruding non-globular dendrite. In each case, the triangle
16 signifies a crystalline impurity particle, which is observed to be the nucleating site
17 for defective deposition.

1

1

2 The deposition of protruding lithium defects was observed at current densities greater than $i = 0.04$
3 mA cm^{-2} . The three kinds of defective lithium deposition that we will report in this paper are shown
4 schematically in Fig. 3. All of the defects are nucleated on crystalline impurities. We hypothesize that
5 the impurities are crystals of Li_3N or Li_2O . All of the impurities expected in lithium metal are electronic
6 insulators, and we thus expect them to have similar effects on lithium deposition. In Fig. 3a, we show a
7 void defect, wherein lithium deposition is suppressed in the vicinity of the impurity due to its insulating
8 character. Fig. 3b shows a globular protrusion. This is attributed to local disruption of the solid
9 electrolyte interphase in the vicinity of the impurity. Fig. 3c shows a non-globular, branched structure
10 nucleated at an impurity - this shape most closely resembles the classical dendrite. The depictions in
11 Fig. 3 are based on data we will present shortly, and build on previous studies by Harry et al.^{35,36}

12 Figure 4 shows examples of defective lithium deposition inside **failed** cells observed by X-ray
13 tomography. In Fig. 4a, X-ray tomography results obtained at $i = 0.08 \text{ mA cm}^{-2}$ are shown. **This cell**
14 **failed at $C_d = 50.1 \text{ C cm}^{-2}$, corresponding to 68 microns of lithium deposition.** Most of the defects at this
15 current density are voids, and lithium deposition is planar. Fig. 4b shows X-ray tomography results
16 obtained at $i = 0.32 \text{ mA cm}^{-2}$. **This cell failed at $C_d = 18.7 \text{ C cm}^{-2}$, corresponding to 25 microns of**
17 **lithium deposition.** Here we see the formation of a globular defect. At intermediate current densities
18 such as $i = 0.32 \text{ mA cm}^{-2}$, we observe both voids and globular defects. In Fig. 4c, X-ray tomography
19 results obtained at $i = 0.64 \text{ mA cm}^{-2}$ are shown. **This cell failed at $C_d = 0.92 \text{ C cm}^{-2}$, corresponding to 1.2**
20 **microns of lithium deposition.** Here, we see the formation of a non-globular dendrite. The protrusion
21 shown exhibits branching and a small tip radius. At this current density, we observe voids, globular
22 defects, and non-globular dendrites. Despite the relatively large current density, all protrusions were

1

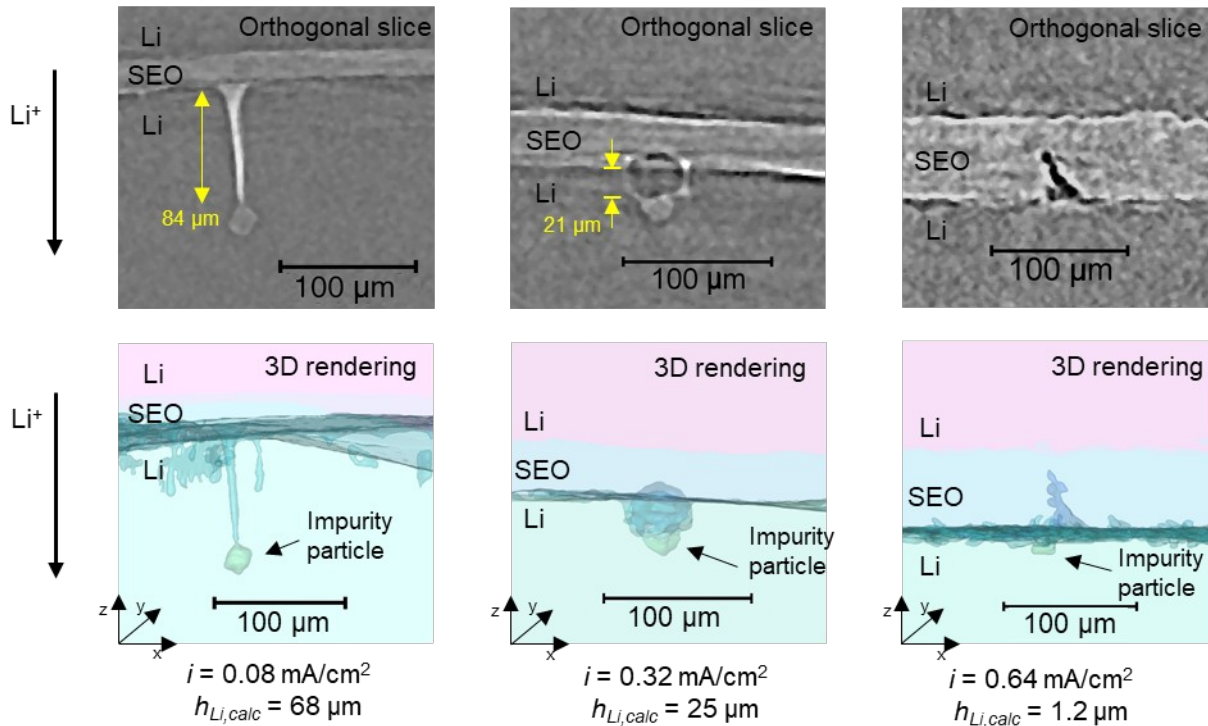
1 observed to nucleate at an impurity particle. Figures 3 and 4 are parallel to each other: Figure 4 shows
2 data corresponding to the idealized schematics in Figure 3.

3 We observed two classes of failures in short-circuited cells. We refer to the first class as defect-driven
4 failure: an example is shown in Fig. 5a, where we show X-ray tomography results of a cell polarized at i
5 = 0.32 mA cm⁻². In this class, we observe an electrolyte-spanning protrusion nucleated on an impurity
6 particle. We refer to the second class as fabrication-related failure: an example is shown in Fig. 5b,
7 where we show results from a cell polarized at $i = 0.08$ mA cm⁻². In this class, the cell contains no
8 protrusion defects (either globular or non-globular). Instead, we see a break in the electrolyte layer and a
9 concomitant merging of the top and bottom electrodes. It is reasonable to expect that the electrolyte
10 thickness in our cells is not perfectly uniform. We posit that the cell failure mode shown in Fig. 5b
11 occurs due to a local thin spot in the electrolyte membrane. The impurity particles in Fig. 5b result in the
12 formation of void defects, which do not adversely affect cell lifetime. Note that the length scale of the
13 two kinds of failures is very different: protrusions are tens of microns wide, while fabrication-related
14 failures extend across hundreds of microns.

15 At $i = 0.08$ mA cm⁻², we observed two populations of cells with very different lifetimes. Cells that
16 contained signatures of defect-driven failure (i.e., a globular defect nucleated on an
17 impurity particle) exhibited an average lifetime of 10 hours. In contrast, cells that contained
18 signatures of fabrication-related failure exhibited an average lifetime of 181 hours. The deleterious
19 effect of dendrite growth on cell lifetime is clear. At $i \geq 0.16$ mA cm⁻², all cells exhibited defect-driven
20 failure.

21

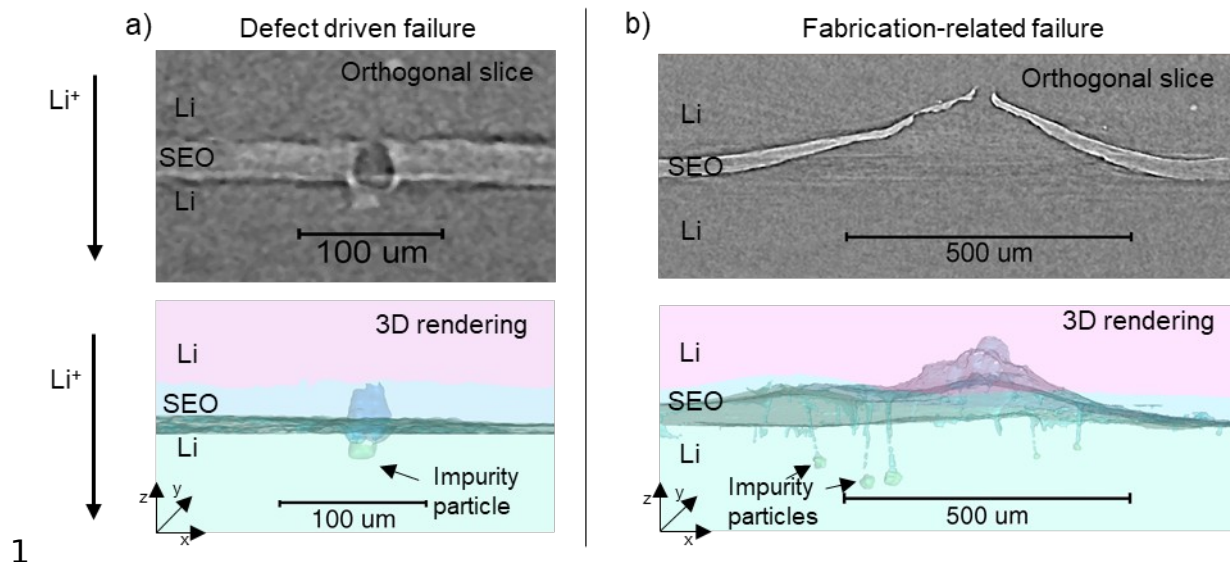
1
2



3

4Figure 4. Examples of defective lithium deposition observed in this study by X-ray tomography. The
5top row shows an orthogonal cross-section through the defect. The bottom row shows a 3D rendered
6volume that includes the defect. In the 3D rendering, the lower interface between electrolyte and lithium
7is highlighted. The impurity particle, present in each tomogram, is colored green. Lithium is deposited
8from top to bottom. The current densities used to polarize the cells are indicated, along with the
9calculated average thickness of lithium, $h_{Li,calc}$, deposited on the bottom electrode. The yellow arrows are
10used to estimate the actual thickness of lithium deposited, using the impurity particle as a reference
11point. In the third cell, not enough lithium was deposited to label the figure. (a) a void defect, (b) a
12protruding lithium globule, and (c) a protruding non-globular dendrite.

1



2Figure 5. Comparison of defect-driven and fabrication-related modes of cell failure. The top row shows

3an orthogonal cross-section through the defect. The bottom row shows a 3D rendered volume that

4includes the defect. In the 3D rendering, the lower interface between electrolyte and lithium is

5highlighted. (a) A cell polarized at $i = 0.32 \text{ mA cm}^{-2}$ was short-circuited at $t = 0.7 \text{ h}$ and **an average of**

6 $1.1 \text{ } \mu\text{m}$ of lithium plated due to the formation of a lithium globule. (b) A cell polarized at $i = 0.08 \text{ mA}$

7 cm^{-2} was short-circuited at $t = 174 \text{ h}$ and **an average of** $68 \text{ } \mu\text{m}$ of lithium plated when lithium deposited

8preferentially through a local thin spot in the polymer electrolyte.

9

10

1

Table 2. Cell lifetime and defect density in failed cells as a function of current density.

<i>Current Density, i</i> [mA cm ⁻²]	<i>Average C_d</i> [C cm ⁻²]	<i>Average void density,</i> <i>V</i> [mm ⁻²]	<i>Average protrusion density,</i> <i>P</i> [mm ⁻²]	<i>Average defect density, (V</i> <i>+ P)</i> [mm ⁻²]
0.04	129.6*		0	
0.08	31.2	2.2	0.11	2.3
0.16	13.05	1.3	0.77	2.1
0.32	7.18	1.8	1.0	2.8
0.64	1.29	1.4	2.1	3.5

*These cells did not fail in spite of galvanostatic polarization for 900 hours. Thus, the reported value of C_d at this current density may be considered as the lower limit.

4 The morphology and density of defects are correlated to current density. After imaging a failed
5 symmetric cell by X-ray tomography, the number of defects per unit area counted manually. At each
6 current density, we examined 3 independent cells except at $i=0.64$ mA/cm² where we examined 2 cells.
7 In each cell an area of 8.7 mm² was examined, which was the entire field of view at the magnification
8 chosen (5X). Our observation of defects is thus based on 11 independent cells with a total area of 113
9 mm². (We ran a total of XX cells. In spite of our best effort to maintain the same instrument
10 configuration, some of the tomograms were not as clear as others. For quantification of defect types, we
11 thus chose the 11 cells with the clearest tomograms.) In Table 2, we quantify our observations by
12 reporting the areal density of each defect type observed in failed cells as a function of current density.
13 Non-globular dendrites are only observed at the highest current density ($i = 0.64$ mA cm⁻²). While some
14 of the observed defects at this current density were clearly dendritic, as shown in Figure 4c, others were
15 globular. Below this current density, all of the protruding defects observed were globular. We use the
16 symbol P to quantify the areal density of protruding defects, both globular and non-globular. We use the
17 symbol V to quantify the areal density of void defects. The dependence of P and V on i is presented in

1 Table 2. Generally, void density decreases slightly with increasing current density. (Average void
2 density was not calculated at $i = 0.04 \text{ mA cm}^{-2}$ because the cells did not fail.) In contrast, protrusion
3 density increases significantly with increasing current density. Since both void and protrusion defects
4 are nucleated at impurities, one might expect this sum to be related to the number density of impurity
5 particles in the lithium electrode. This is consistent with our observation that $(V + P)$ is weakly
6 correlated to current density (see Table 2).

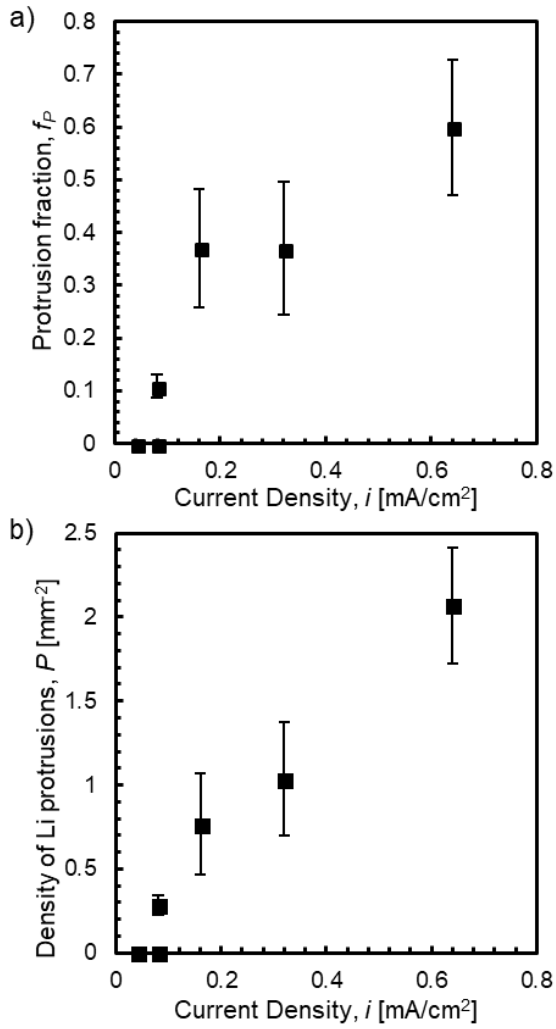
7 In Figure 6a, we show that P is a monotonically increasing function of i . At $i = 0.04 \text{ mA cm}^{-2}$, $P = 0$,
8 i.e., no globules or non-globular dendrites were observed at this current density. At $i = 0.08 \text{ mA cm}^{-2}$,
9 we observe two populations of cells: some cells exhibited globular defects, while others did not. The
10 two data points at this current density in Fig. 6a reflect this fact. At higher current densities, all cells
11 exhibited protruding defects. In Figure 6b, we plot the fraction of protruding defects, f_p , defined as

12

13

$$\text{Protrusion fraction, } f_p = \frac{P}{V+P} \quad (1)$$

14 as a function of i . The data in Fig. 6a and 6b indicate that the probability of nucleating protrusion
15 defects at impurities increases with increasing current density.

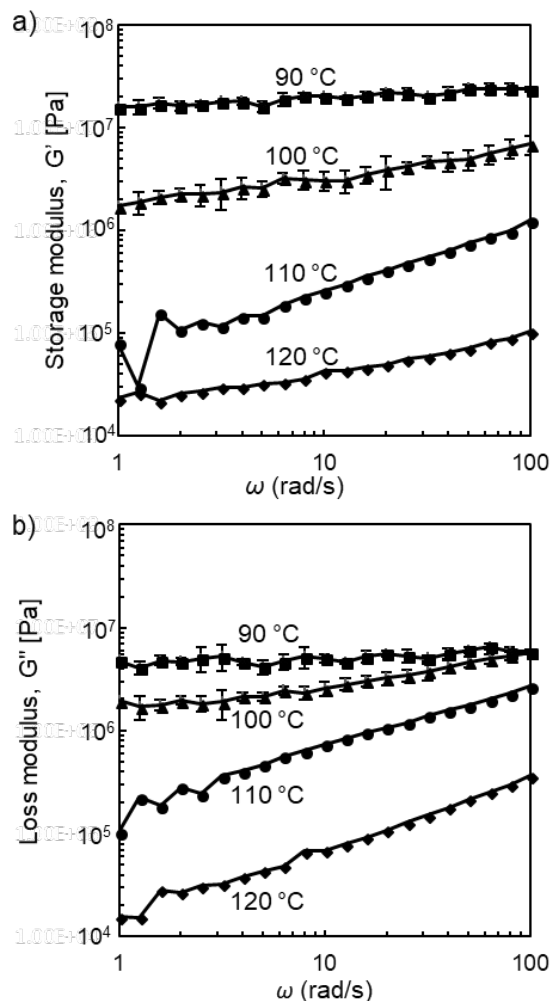


1

2Figure 6. Correlation between current density and defect density in failed cells. (a) The areal density of
 3protruding defects, P , increases with current density. (b) The protrusion fraction, f_p , also increases with
 4current density.

5

1

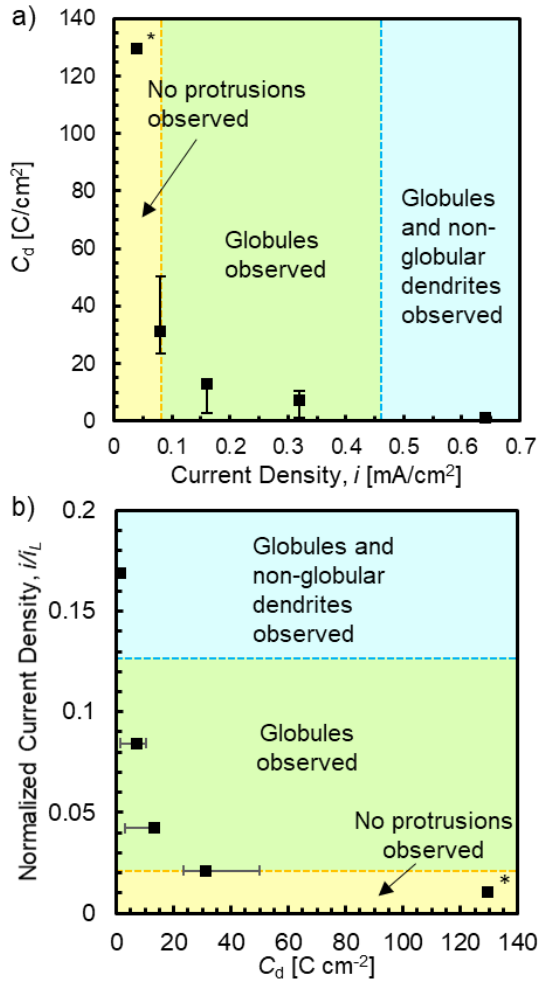


1
 2 **Figure 7.** Frequency dependence of shear (a) storage, G' , and (b) loss, G'' , moduli measured at 90, 100, 110, and 120 °C. Error bars represent 3 measurements taken and averaged at 100 °C and 90 °C, the temperature of interest.

5 Fig. 7a and 7b show the measured shear storage (G') and loss (G'') moduli, respectively, of the polymer used in this study at a range of temperatures from 90 – 120 °C. At 90 °C, the temperature of interest, G' is nearly independent of frequency (about 2×10^7 Pa), and G' is a factor of 5 larger than G'' . These are signatures of an elastic solid. Monroe and Newman first proposed that the parameter that governs lithium dendrite growth is the ratio of the shear moduli of separator and electrode, here the SEO electrolyte and lithium metal, $G^{\text{SEO}}/G^{\text{Li}}$.²⁹ We have used the 3.4 GPa value as G^{Li} , identical to that used

1 by Barai et al. and Monroe and Newman, to calculate this ratio.^{29,30} $G^{\text{SEI}} = 0.02$ GPa, the low frequency
2 value of G' at 90 °C. In principle, we should use the shear modulus of a lithium metal protrusion at 90
3 °C. To our knowledge, the shear modulus of lithium at 90 °C has not yet been reported; however, there
4 is evidence that the shear modulus will have a weak dependence on temperature.³⁸ It is important to
5 recognize that recent work by Xu et al.³⁸ and Herbert et al.³⁹ suggests that the modulus of lithium
6 dendrites may be substantially higher than that of bulk lithium metal and have a strong dependence on
7 crystallographic orientation, a complication that was not included in the work of Monroe and Newman
8 and Barai et al. All of these complications notwithstanding, we compare our results with the
9 simulations of Barai et al., who predicted the stability of lithium deposition as a function of i and $G^{\text{SEI}}/$
10 G^{Li} .³⁰

11



1

2

3 **Figure 8.** Nature of observed lithium protrusions as a function of current density, i , and charge passed
 4 before failure, C_d . Observation of no protrusion nucleation at low current densities (yellow area),
 5 globules at medium current densities (green area) and non-globular dendrites at high current densities
 6 (blue area). The asterisk at $i = 0.04$ mA cm⁻² indicates these cells had not failed at the time point used to
 7 calculate C_d , ($t = 900$ h). (a) C_d as a function of i . (b) Normalized current density, i/i_L , as a function of
 8 C_d , where i_L is theoretical limiting current (Eq. 2)²⁸.

9

10

1

Table 3. Parameters used to estimate limiting current.

<i>Parameter</i>	<i>Value</i>
c , bulk concentration of salt in the PEO domains of the electrolyte ⁴⁰	$1.66 \times 10^{-3} \left[\frac{\text{mol}}{\text{cm}^3} \right]$
D , salt diffusion coefficient ⁴⁰	$4.5 \times 10^{-8} \left[\frac{\text{cm}^2}{\text{s}} \right]$
L , electrolyte thickness	$40 \times 10^{-4} [\text{cm}]$
t_{Li} , transference number of the lithium ion ⁴⁰	0.05

2
3 Fig. 8a describes the effect of current density on the nature of lithium deposition, using Fig. 1b as the
4basis. At very low current densities, protrusion nucleation and growth is suppressed and no defect-
5driven failures are observed. At intermediate current densities, partial suppression leads to the
6observation of lithium globules. At high current densities, globular and non-globular dendrites are
7observed, along with extremely short cell lifetimes. Fig. 8b recasts C_d as a function of normalized
8current density, i/i_L . Normalized current density is defined as the current density applied to the cell
9divided by the theoretical limiting current as defined by Monroe and Newman (Eq. 2).²⁸ The parameters
10used to calculate i_L are given in Table 3.

$$i_L = \frac{2cDF}{L(1-t_{Li})} \approx 3.8 \text{ mA cm}^{-2} \quad (2)$$

11 The qualitative trend demonstrated in Fig. 8 by experiment is consistent with the trend calculated
12theoretically by Barai et al., who predicted stable lithium deposition at low current densities and
13unstable lithium deposition at high current densities. The predicted value of i/i_L at the crossover between
14stable and unstable deposition for $G^{\text{SEO}}/G^{\text{Li}} \approx 0.006$ (we use $G^{\text{Li}} \approx 3.4 \text{ GPa}$ and $G^{\text{SEO}} = 0.02 \text{ GPa}$) is about
150.39. (Using the $G^{\text{Li}} \approx 9 \text{ GPa}$ value suggested by Xu et al. for (100) Li pillars leads to a crossover $i/i_L \approx$
160.32 which is not very different from 0.39 determined above.)³⁸ In contrast, the experimentally
17determined value of i/i_L at this crossover is about 0.02. The experimentally determined crossover from

1 globular to dendritic protrusions, which occurs at i/i_L of about 0.13, is also significantly lower than
2 theoretical prediction. Three possible reasons for the discrepancy between theory and experiment are:
3 (1) The theoretical model applies to lithium metal anodes devoid of impurities, while our experiments
4 suggest that impurities play an important role. It is conceivable that the current distributions in our
5 experimental cells in the vicinity of the impurities are very different from those in the model. (2) The
6 theoretically predicted limiting current density based on Eq. 2 may be significantly different from the
7 practical limiting current density, due to factors, such as ion transport parameters and block copolymer
8 microstructure, that are highly dependent on salt concentration.⁴¹ (3) The shear modulus of lithium used
9 to make the theoretical calculation, 3.4 GPa, does not take into account geometry and crystallographic
10 orientation, and may not reflect the mechanical properties of the lithium protrusion.

11

12 CONCLUSION

13 The effect of current density on defective lithium deposition in symmetric lithium-polymer-lithium
14 cells was studied by X-ray microtomography. We are particularly interested in the growth of
15 protrusions, which are either globular or dendritic. These defects were nucleated on insulating impurity
16 particles in the lithium electrode. At low current densities ($i = 0.04 \text{ mA cm}^{-2}$), planar lithium deposition
17 without protrusions is observed. As current density increases ($0.08 \leq i \leq 0.32 \text{ mA cm}^{-2}$), globular
18 protrusions are obtained. At the highest current density ($i = 0.64 \text{ mA cm}^{-2}$), globular and dendritic
19 protrusions are obtained. The areal density of protrusions increases monotonically with increasing
20 current density. The lifetime of the symmetric cell correlates with the areal density of protrusions. Our
21 experimental findings were compared to the theoretical predictions of Barai et al.³⁰, using the measured
22 modulus of the polymer and an estimate for the limiting current density, without resorting to any
23 additional adjustable parameters. The experimentally determined onset of non-planar lithium deposition

1 occurred at a current density about a factor of **twenty** lower than that predicted by Barai et al. An
2 important limitation of current lithium electrodes is the presence of numerous impurity particles. It is
3 conceivable that the current density range over which planar lithium deposition occurs would increase
4 dramatically if such electrodes were available. We hope that our work will motivate the manufacture of
5 such electrodes in the near future.

6

7 AUTHOR INFORMATION

8 Corresponding Author

9 *nbalsara@berkeley.edu

10

11 Notes

12 The authors declare no competing financial interest.

13 ACKNOWLEDGMENTS

14 This work was supported by the Assistant Secretary for Energy Efficiency and Renewable Energy,
15 Office of Vehicle Technologies of the U.S. Department of Energy under Contract DE-AC02-05CH11231
16 under the Battery Materials Research Program. Hard X-ray experiments were performed at the
17 Advanced Light Source which is supported by the Director, Office of Science, Office of Basic Energy
18 Sciences, of the U.S. Department of Energy under Contract No. DE-AC02-05CH11231. JAM was
19 supported by a National Science Foundation Graduate Research Fellowship (DGE 2752814).

20

1 REFERENCES

- 2(1) Xu, W.; Wang, J.; Ding, F.; Chen, X.; Nasybulin, E.; Zhang, Y.; Zhang, J.-G. Lithium Metal
3 Anodes for Rechargeable Batteries. *Energy Environ. Sci.* **2014**, *7*, 513–537.
- 4(2) Choi, J. W.; Aurbach, D. Promise and Reality of Post-Lithium-Ion Batteries with High Energy
5 Densities. *Nat. Rev. Mater.* **2016**, *1*, 1–16.
- 6(3) Mizushima, K.; Jones, P. C.; Wiseman, P. J.; Goodenough, J. B. Li_xCoO_2 ($0 < x \leq 1$): A New
7 Cathode Material for Batteries of High Energy Density. *Solid State Ionics* **1981**, *3–4*, 171–174.
- 8(4) Tarascon, J.-M.; Armand, M. Issues and Challenges Facing Rechargeable Lithium Batteries.
9 *Nature* **2001**, *414*, 359–367.
- 10(5) Zhang, J.-G.; Wu, X.; Henderson, W. A. *Springer Series in Materials Science: Lithium Metal*
11 *Anodes and Rechargeable Lithium Metal Batteries*; Springer International Publishing AG
12 Switzerland, 2017.
- 13(6) Balsara, N. P.; Newman, J. Comparing the Energy Content of Batteries, Fuels, and Materials. *J.*
14 *Chem. Educ.* **2013**, *90*, 446–452.
- 15(7) Takeda, Y.; Yamamoto, O.; Imanishi, N. Lithium Dendrite Formation on a Lithium Metal Anode
16 from Liquid, Polymer and Solid Electrolytes. *Electrochemistry* **2016**, *4*, 210–218.
- 17(8) Lin, D.; Liu, Y.; Cui, Y. Reviving the Lithium Metal Anode for High-Energy Batteries. *Nat.*
18 *Nanotechnol.* **2017**, *12*, 194–206.
- 19(9) Aurbach, D.; Zinigrad, E.; Cohen, Y.; Teller, H. A Short Review of Failure Mechanisms of
20 Lithium Metal and Lithiated Graphite Anodes in Liquid Electrolyte Solutions. *Solid State Ionics*
21 **2002**, *148*, 405–416.
- 22(10) Arakawa, M.; Tobishima, S.; Nemoto, Y.; Ichimura, M.; Yamaki, J. Lithium Electrode

- 1 Cycleability and Morphology Dependence on Current Density. *J. Power Sources* **1993**, 43–44,
2 27–35.
- 3(11) Aurbach, D.; Zinigrad, E.; Teller, H.; Dan, P. Factors Which Limit the Cycle Life of
4 Rechargeable Lithium (Metal) Batteries. *J. Electrochem. Soc.* **2000**, 147, 1274-1279.
- 5(12) Brissot, C.; Rosso, M.; Chazalviel, J.-N.; Baudry, P.; Lascaud, S. *In Situ* Study of Dendritic
6 Growth in Lithium/PEO-Salt/Lithium Cells. *Electrochim. Acta* **1998**, 43, 1569–1574.
- 7(13) Brissot, C.; Rosso, M.; Chazalviel, J.-N.; Lascaud, S. *J. In Situ* Concentration Cartography in the
8 Neighborhood of Dendrites Growing in Lithium/Polymer-Electrolyte/Lithium Cells.
9 *Electrochem. Soc.* **1999**, 146, 4393-4400.
- 10(14) Zhang, X.-W.; Li, Y.; Khan, S. A.; Fedkiw, P. S. Inhibition of Lithium Dendrites by Fumed
11 Silica-Based Composite Electrolytes. *J. Electrochem. Soc.* **2004**, 151, A1257-A1263.
- 12(15) Liu, S.; Imanishi, N.; Zhang, T.; Hirano, A.; Takeda, Y.; Yamamoto, O.; Yang, J. Lithium
13 Dendrite Formation in Li/Poly(ethylene oxide)-Lithium Bis(trifluoromethanesulfonyl)imide and
14 *N*-Methyl-*N*-propylpiperidinium Bis(trifluoromethanesulfonyl)imide/Li cells. *J. Electrochem.*
15 *Soc.* **2010**, 157, A1092-A1098.
- 16(16) Nagao, M.; Hayashi, A.; Tatsumisago, M.; Kanetsuku, T.; Tsuda, T.; Kuwabata, S. *In Situ* SEM
17 Study of a Lithium Deposition and Dissolution Mechanism in a Bulk-Type Solid-State Cell with
18 a Li₂S-P₂S₅ Solid Electrolyte. *Phys. Chem. Chem. Phys.* **2013**, 15, 18600–18606.
- 19(17) Porz, L.; Swamy, T.; Sheldon, B. W.; Rettenwander, D.; Frömling, T.; Thaman, H. L.; Berendts,
20 S.; Uecker, R.; Carter, W. C.; Chiang, Y. M. Mechanism of Lithium Metal Penetration through
21 Inorganic Solid Electrolytes. *Adv. Energy Mater.* **2017**, 7, 1–12.
- 22(18) Cheng, E. J.; Sharafi, A.; Sakamoto, J. Intergranular Li Metal Propagation through

- 1 Polycrystalline $\text{Li}_{6.25}\text{Al}_{0.25}\text{La}_3\text{Zr}_2\text{O}_{12}$ Ceramic Electrolyte. *Electrochim. Acta* **2017**, *223*, 85–91.
- 2(19) Schausser, N. S.; Harry, K. J.; Parkinson, D. Y.; Watanabe, H.; Balsara, N. P. Lithium Dendrite
3 Growth in Glassy and Rubbery Nanostructured Block Copolymer Electrolytes. *J. Electrochem.*
4 *Soc.* **2015**, *162*, 398–405.
- 5(20) Tatsuma, T.; Taguchi, M.; Oyama, N. Inhibition Effect of Covalently Cross-Linked Gel
6 Electrolytes on Lithium Dendrite Formation. *Electrochim. Acta* **2001**, *46*, 1201–1205.
- 7(21) Stone, G. M.; Mullin, S. A.; Teran, A. A.; Hallinan, D. T.; Minor, A. M.; Hexemer, A.; Balsara,
8 N. P. Resolution of the Modulus versus Adhesion Dilemma in Solid Polymer Electrolytes for
9 Rechargeable Lithium Metal Batteries. *J. Electrochem. Soc.* **2012**, *159*, A222-A227.
- 10(22) Ding, F.; Xu, W.; Graff, G. L.; Zhang, J.; Sushko, M. L.; Chen, X.; Shao, Y.; Engelhard, M. H.;
11 Nie, Z.; Xiao, J.; Liu, X.; Sushko, P. V.; Liu, J.; Zhang, J. G. Dendrite-Free Lithium Deposition
12 via Self-Healing Electrostatic Shield Mechanism. *J. Am. Chem. Soc.* **2013**, *135*, 4450–4456.
- 13(23) Bouchet, R.; Maria, S.; Meziane, R.; Aboulaich, A.; Lienafa, L.; Bonnet, J.; Phan, T. N. T.;
14 Bertin, D.; Gigmes, D.; Devaux, D.; Denoyel, R.; Armand, M. Single-Ion BAB Triblock
15 Copolymers as Highly Efficiency Electrolytes for Lithium-Metal Batteries. *Nat. Mater.* **2013**, *12*,
16 452–457.
- 17(24) Khurana, R.; Schaefer, J. L.; Archer, L. A.; Coates, G. W. Suppression of Lithium Dendrite
18 Growth Using Cross-Linked Polyethylene/Poly(ethylene oxide) Electrolytes: A New Approach
19 for Practical Lithium-Metal Polymer Batteries. *J. Am. Chem. Soc.* **2014**, *136*, 7395–7402.
- 20(25) Villaluenga, I.; Wujcik, K. H.; Tong, W.; Devaux, D.; Wong, D. H. C.; DeSimone, J. M.;
21 Balsara, N. P. Compliant Glass-Polymer Hybrid Single Ion-Conducting Electrolytes for Lithium
22 Batteries. *Proc. Natl. Acad. Sci. U. S. A.* **2015**, *113*, 52–57.

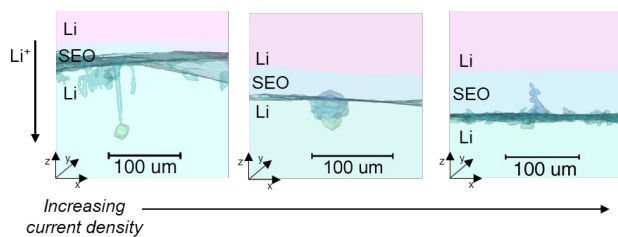
- 1(26) Manuel Stephan, A.; Nahm, K. S. Review on Composite Polymer Electrolytes for Lithium
2 Batteries. *Polymer*. **2006**, *47*, 5952–5964.
- 3(27) Gilbert, J. B.; Luo, M.; Shelton, C. K.; Rubner, M. F.; Cohen, R. E.; Epps III, T. H.
4 Determination of Lithium-Ion Distributions in Nanostructured Block Polymer Electrolyte Thin
5 Films by X-ray Photoelectron Spectroscopy Depth Profiling. *ACS Nano* **2015**, *9*, 512–520.
- 6(28) Monroe, C.; Newman, J. Dendrite Growth in Lithium/Polymer Systems. *J. Electrochem. Soc.*
7 **2003**, *150*, A1377-A1384.
- 8(29) Monroe, C.; Newman, J. The Impact of Elastic Deformation on Deposition Kinetics at
9 Lithium/Polymer Interfaces. *J. Electrochem. Soc.* **2005**, *152*, A396-A404.
- 10(30) Barai, P.; Higa, K.; Srinivasan, V. Lithium Dendrite Growth Mechanisms in Polymer Electrolytes
11 and Prevention Strategies. *Phys. Chem. Chem. Phys.* **2017**, *19*, 20493–20505.
- 12(31) Barai, P.; Higa, K.; Srinivasan, V. Effect of Initial State of Lithium on the Propensity for
13 Dendrite Formation: A Theoretical Study. *J. Electrochem. Soc.* **2017**, *164*, 180–189.
- 14(32) Quirk, R. P.; Kim, J.; Kausch, C.; Chun, M. Butyllithium-Initiated Anionic Synthesis of Well-
15 Defined Poly(styrene-*block*-ethylene oxide) Block Copolymers with Potassium Salt Additives.
16 *Polym. Int.* **1996**, *39*, 3–10.
- 17(33) Hadjichristidis, N.; Iatrou, H.; Pispas, S.; Pitsikalis, M. Anionic Polymerization: High Vacuum
18 Techniques. *J. Polym. Sci. Part A: Polym. Chem.* **2000**, *38*, 3211–3234.
- 19(34) Singh, M.; Odusanya, O.; Wilmes, G. M.; Eitouni, H. B.; Gomez, E. D.; Patel, A. J.; Chen, V. L.;
20 Park, M. J.; Fragouli, P.; Iatrou, H. et al. Effect of Molecular Weight on the Mechanical and
21 Electrical Properties of Block Copolymer Electrolytes. *Macromolecules* **2007**, *40*, 4578–4585.
- 22(35) Harry, K. J.; Hallinan, D. T.; Parkinson, D. Y.; Macdowell, A. A.; Balsara, N. P. Detection of

- 1 Subsurface Structures Underneath Dendrites Formed on Cycled Lithium Metal Electrodes. *Nat.*
2 *Mater.* **2013**, *13*, 69–73.
- 3(36) Harry, K. J.; Liao, X.; Parkinson, D. Y.; Minor, A. M.; Balsara, N. P. Electrochemical Deposition
4 and Stripping Behavior of Lithium Metal across a Rigid Block Copolymer Electrolyte
5 Membrane. *J. Electrochem. Soc.* **2015**, *162*, A2699–A2706.
- 6(37) Harry, K. J.; Higa, K.; Srinivasan, V.; Balsara, N. P. Influence of Electrolyte Modulus on the
7 Local Current Density at a Dendrite Tip on a Lithium Metal Electrode. *J. Electrochem. Soc.*
8 **2016**, *163*, 2216–2224.
- 9(38) Xu, C.; Ahmad, Z.; Aryanfar, A.; Viswanathan, V.; Greer, J. R. Enhanced Strength and
10 Temperature Dependence of Mechanical Properties of Li at Small Scales and Its Implications for
11 Li Metal Anodes. *Proc. Natl. Acad. Sci. U. S. A.* **2017**, *114*, 57–61.
- 12(39) Herbert, E. G.; Hackney, S. A.; Dudney, N. J.; Thole, V.; Phani, P. S. Nanoindentation of High-
13 Purity Vapor Deposited Lithium Films: A Mechanistic Rationalization of the Transition from
14 Diffusion to Dislocation-Mediated Flow. *J. Mater. Res.* **2018**, *33*, 1346–1359.
- 15(40) Villaluenga, I.; Pesko, D. M.; Timachova, K.; Feng, Z.; Newman, J.; Srinivasan, V.; Balsara, N.
16 P. Negative Stefan-Maxwell Diffusion Coefficients and Complete Electrochemical Transport
17 Characterization of Homopolymer and Block Copolymer Electrolytes. **2018**, *165*, 2766–2773.
- 18(41) Pesko, D. M.; Timachova, K.; Bhattacharya, R.; Smith, M. C.; Villaluenga, I.; Newman, J.;
19 Balsara, N. P. Negative Transference Numbers in Poly(ethylene oxide)-Based Electrolytes. *J.*
20 *Electrochem. Soc.* **2017**, *164*, E3569–E3575.

21

1

TOC graphic



2

1